1	
2	Sea Level Variability over the Northwest European Shelf across Different Timescale
3	
4	Yueyang Lu, Xiaobiao Xu, Eric P. Chassignet
5	Center for Ocean-Atmospheric Prediction Studies, Florida State University
6	Tallahassee, Florida
7	

Abstract

We examine the sea level variability over the Northwest European Shelf (NWES) across different timescales and its underlying drivers. Using a basin-scale Atlantic Ocean model that accurately reproduces the NWES sea level variability compared with observations, we separate the sea level change into interannual, seasonal, intraseasonal, and high-frequency (less than 10 days) components. The seasonal, intraseasonal, and high-frequency variabilities exhibit comparable magnitudes, whereas interannual variability contributes a smaller fraction of the total sea level variation. We further decompose the shelf sea level change into contributions from mass and steric (density) changes. Our analysis shows that the steric change only contributes to the seasonal cycle of the NWES sea level variability, primarily driven by surface heat transport rather than lateral one. In contrast, lateral mass transport induced by winds onto the shelf accounts for most of the variability on seasonal, intraseasonal, and high-frequency timescales. The mass transport contribution is strongly correlated with regional wind stresses across all timescales, which is explained by the Ekman transport mechanism. These correlations, however, exhibit distinct spatial patterns depending on the timescale considered.

24 Key points:

- The Northwest European Shelf sea level shows pronounced variability over a range of timescales, especially sub-annual ones.
- The steric sea level component contributes mainly to the seasonal cycle, controlled by surface heat fluxes.
- The mass component accounts for most of the variability and is correlated with regional winds, though the correlation pattern varies across timescales.

Plain Language Summary

Sea level along the Northwest European Shelf (NWES) changes on many timescales — from days to years — and is influenced by different physical processes. Using a high-resolution ocean model that closely matches satellite observations, we examined how and why sea level varies in this region. We found that short-term variations, from a few days to a few months, are much stronger than the slower, year-to-year changes. Most of these sea level fluctuations are caused by the movement of water driven by winds pushing water onto or away from the shelf. Changes in seawater density (caused by heating or cooling) also affect the sea level, but mainly explain the seasonal fluctuation of the sea level and are mostly due to ocean surface heat transport. Overall, our study shows that winds and the resulting water movements are the main drivers of sea level variability over the NWES at most timescales.

1. Introduction

Global sea level has been rising since the late 19th century, primarily due to ocean thermal expansion and melting of land ice. Recent estimates indicate that by 2020, global mean sea level was 200–230 mm higher than in 1900 (Church and White, 2011; Frederikse et al., 2020). The rate of rise has not been constant and has accelerated in recent decades. Since the advent of satellite altimetry in 1993, the global mean sea level rise has reached ~4.5 mm/yr, more than twice the 20th-century average (Church and White, 2011; Beckley et al., 2017; Frederikse et al., 2020; Hamlington et al., 2024). Superimposed on this long-term trend, the sea level exhibits variability from intraseasonal to decadal timescales, driven by large-scale ocean—atmosphere interactions and climate modes, and these variations are spatially heterogeneous. Continental shelves, in particular, display distinct sea level variability characteristics compared to the open ocean (Steinberg et al., 2024).

The Northwest European Shelf (NWES; Figure 1) is a key coastal region influenced by the easternmost branch of the North Atlantic Current, the European Slope Current, which flows through the Rockall Trough along the shelf's western margin (Souza et al., 2000; Hansen and Østerhus, 2000; Xu et al., 2015; Fraser et al., 2022). This slope current modifies along-shelf

density and pressure gradients through exchanges between the open ocean and the shelf, linking the NWES sea level to broader North Atlantic circulation (Huthnance et al., 2022; Diabaté et al., 2025). The NWES is also relatively shallow, and its hydrographic response to global warming differs from that of the open subpolar North Atlantic (Wakelin et al., 2009; Holt et al., 2010; Tinker et al., 2024).

The NWES sea level varies across multiple timescales. The long-term trend indicates a rise of 3.1 mm/yr since 1993 (Melet et al., 2024), projected to accelerate under future climate scenarios due to changes in ocean density and local mass convergence or divergence (steric and manometric effects, respectively; Gregory et al., 2019; Weeks et al., 2023). Superimposed on this trend, the NWES sea level exhibits decadal to intraseasonal variability, primarily driven by manometric changes associated with ocean currents and winds. The decadal variability is strongly linked to large-scale atmospheric patterns such as the North Atlantic Oscillation, the East Atlantic Pattern, and Scandinavian teleconnection patterns (Tsimplis & Shaw, 2008; Calafat et al., 2012; Chafik et al., 2017). On interannual and shorter timescales, regional wind stress dominates NWES sea level variability by transporting mass onto or off the shelf (Dangendorf, 2014; Hermans et al., 2020; Wise et al., 2024; Diabaté et al., 2025). The questions then arise as

to whether wind remains the dominant driver across all timescales and how the magnitude of sea level variability compares in space and time.

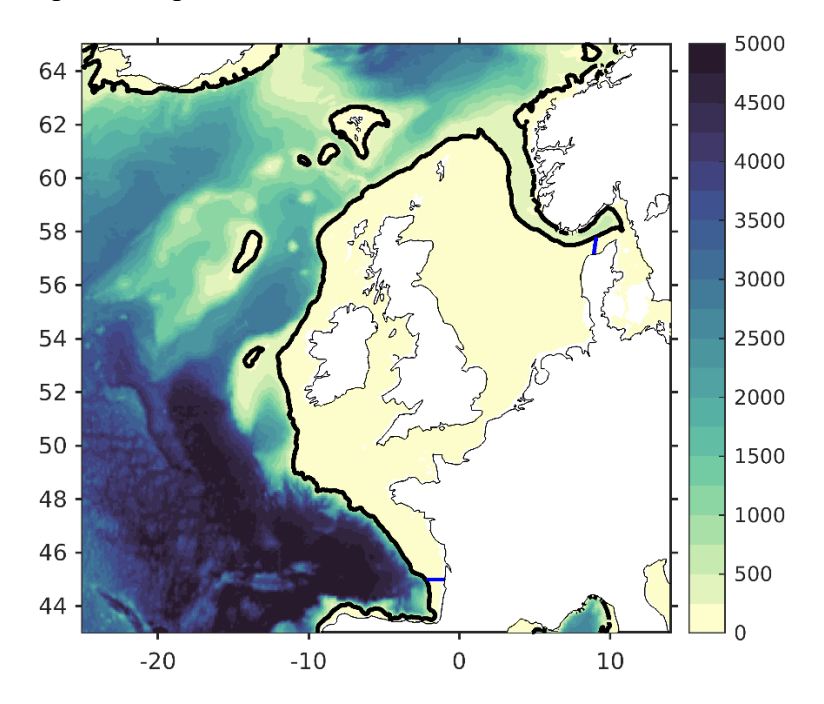


Figure 1. Bathymetry of the eastern subpolar North Atlantic Ocean. The black solid contour line denotes the 200 m isobath. The Northwest European Shelf (NWES) region is defined as the ocean shallower than 200 m, bounded by two transects (blue lines) connecting the coast at 45°N and at 8°E, similar to Wise et al. (2024). Note that the full model domain covers the Equatorial and North Atlantic (Xu et al. 2013, 2018).

In this study, we use a high-resolution numerical ocean model to comprehensively examine the NWES sea level variability from interannual to intraseasonal timescales. We quantify the contribution of wind in driving the manometric change and assess the relative importance of the steric change which has often been considered secondary in previous studies. Our approach is novel in that it simultaneously compares the manometric and steric contributions across all timescales. We find that: (1) the seasonal and shorter-timescale variability is roughly three times larger than interannual and longer-term variability; (2) the steric component is primarily associated with the seasonal cycle, driven by surface heat fluxes; and (3) the manometric component dominates variability across all timescales and is correlated with wind stress, though spatial patterns of the correlations differ, with short-term variability linked to

regional winds and longer-term variability influenced by more remote winds over the subpolar North Atlantic.

The paper is organized as follows. Section 2 describes the ocean model, datasets, and the kinematic equation of sea level evolution. Section 3 presents the results: Section 3.1 compares model sea surface height and circulation with observations; Section 3.2 evaluates sea level variability across timescales; Sections 3.3 and 3.4 examine steric and manometric contributions, respectively; and Section 3.5 discusses the role of the mass transport across lateral boundaries. Section 4 summarizes the conclusions and implications of our findings.

2 Numerical simulation, data, and methods

In this section, we briefly describe the numerical simulation, observational datasets, and methods used to analyze NWES sea-level variability. Figure 1 shows the bathymetry of NWES, defined as regions shallower than 200 m and bounded at ~8°E in the east and 45°N in the south, consistent with Wise et al. (2024).

2.1 Atlantic simulation using HYCOM

The study uses a basin-scale Atlantic Ocean simulation based on the HYbrid Coordinate Ocean Model (HYCOM; Bleck, 2002; Chassignet et al., 2003; Halliwell, 2004). Detailed model configurations are described in Xu et al. (2013, 2018); here we summarize its key aspects. The model domain spans 28°S–80°N, covering the North and Equatorial Atlantic. It has a 1/12° horizontal resolution and a 32-layer hybrid vertical grid: isopycnal in the deep ocean, z-level in the upper ocean, and sigma-coordinate in shallow coastal regions.

The atmospheric forcing is provided by ERA-40 reanalysis (Uppala et al., 2005) for 1978–2001 and by the NCEP Climate Forecast System Reanalysis (CFSR; Saha et al., 2010) for 2002–2022. For this study, we use daily model outputs from 2013–2022 to analyze NWES sea surface height (SSH) variability and its drivers. Monthly SSH fields from 1993–2022 are used to assess model performance on annual and interannual timescales. Hereafter, SSH and sea level are used interchangeably.

The model SSH is evaluated against absolute dynamic topography (ADT) derived from satellite altimetry. We use the gridded Level-4 (L4) ADT dataset from the Copernicus Marine

Service (CMEMS, 2024a) at 0.125° resolution. To focus on dynamical processes (Wise et al., 2024), the ADT dataset removes the inverse barometer effect due to low-frequency (>20 days) atmospheric pressure, which can be a significant source of variability on the European Shelf (Hermans et al., 2020). Since the model also excludes this effect, direct comparison between modeled SSH and ADT is appropriate. We further use the CNES-CLS-2022 mean dynamic topography (MDT), representing the 1993–2012 mean sea surface height above the geoid (Jousset et al., 2022; CMEMS, 2024b).

2.2 Evolution of the sea surface height

The SSH change, denoted as η , is traditionally decomposed into contributions from changes in ocean mass and density (Gill and Niler, 1973; Piecuch et al., 2022; Wise et al., 2024).:

135
$$\eta = \frac{1}{g\rho_0} p_b - \frac{1}{\rho_0} \int_{-H}^0 (\rho - \rho_0) \, dz \,, \qquad (1)$$

where g is the gravity, ρ_0 is reference density, p_b is bottom pressure, H is ocean depth, and ρ is ocean density. The first term on the right-hand side is the SSH change component due to mass (manometric) change while the second is due to density (steric) change. To investigate the processes contributing to these two components, the corresponding kinematic evolution equation for SSH can be derived (see Griffies and Greatbatch, 2012, for details):

$$\frac{\partial \eta}{\partial t} = -\frac{\nabla \cdot \mathbf{U}^{\rho}}{\bar{\rho}^{z}} + \frac{F_{s}}{\bar{\rho}^{z}} - \frac{(H + \eta)\partial_{t}\bar{\rho}^{z}}{\bar{\rho}^{z}}, \qquad (2)$$

where $\mathbf{U}^{\rho} = \int_{-H}^{0} \rho \mathbf{u} \, dz$ is the vertically integrated horizontal mass flux ([kg m⁻¹ s⁻¹]), \mathbf{u} is horizontal velocity, $\bar{\rho}^z = \frac{1}{H} (\int_{-H}^{0} \rho \, dz)$ is the vertically averaged density, and F_s is the surface mass flux into the ocean ([kg m⁻² s⁻¹]). The first term on the right-hand side represents the contribution of lateral mass transport to regional sea level change. The second term accounts for processes such as evaporation and precipitation, river runoff, and ice melt or formation. The third term corresponds to steric change, which is related to buoyancy (temperature and salinity) fluxes across lateral and surface boundaries. In essence, the equation indicates that sea level rises when mass increases or when the column-averaged density decreases, and vice versa. Note that in HYCOM, the surface mass flux F_s is treated as a virtual salt flux, producing a steric SSH change

rather than a direct mass change. As a result, the surface mass flux contributions to SSH are incorporated within the steric term. The kinematic sea level equation for HYCOM then becomes:

153
$$\frac{\partial \eta}{\partial t} = -\frac{\nabla \cdot \mathbf{U}^{\rho}}{\bar{\rho}^z} - \frac{(H+\eta)\partial_t \bar{\rho}^z}{\bar{\rho}^z}. (3)$$

This formulation will be used in this study, with the manometric and steric components of SSH change defined as follows

156
$$\eta_m = -\int \frac{\nabla \cdot \mathbf{U}^{\rho}}{\overline{\rho}^z} dt$$
, $\eta_s = -\int \frac{(H+\eta)\partial_t \overline{\rho}^z}{\overline{\rho}^z} dt$, respectively. (4)

A common next step is to decompose the steric SSH change, η_s , into contributions from temperature (thermosteric) and salinity (halosteric) changes (e.g., Gill and Niiler 1973; Tsimplis and Rixen 2002; Landerer et al. 2007; Yin et al. 2010; Lu et al. 2025). This requires separating the relative effects of temperature and salinity on density change using the seawater equation of state (EOS), $\rho = \rho(T, S, p_0)$, where T is potential temperature, S is salinity, and p_0 is reference pressure. Applying the chain rule, the time rate of change of the vertically averaged density in η_s can then be expressed as (Piecuch et al., 2019):

164
$$\frac{\partial \bar{\rho}^z}{\partial t} = \frac{1}{H + \eta} \int_{-H}^{0} \left(\frac{\partial \rho}{\partial T} \frac{\partial T}{\partial t} + \frac{\partial \rho}{\partial S} \frac{\partial S}{\partial t} \right) dz.$$
 (5)

For simplicity, we adopt a linear EOS, incorporating the thermal expansion coefficient $\alpha = \frac{\partial \rho}{(\rho \partial T)}$, and the haline contraction coefficient $\beta = \frac{\partial \rho}{(\rho \partial S)}$. Values of α and β are computed at each grid point and time step using model potential temperature and salinity based on the Thermodynamic Equation of Seawater 2010 (TEOS-10) as implemented in the MATLAB "Gibbs Seawater" package (McDougall & Barker, 2011). Using this linear approximation, the time rate of change of the vertically averaged density can then be expressed as:

171
$$\frac{\partial \bar{\rho}^z}{\partial t} \approx -\frac{1}{H+\eta} \int_{-H}^0 \left(\rho \alpha \frac{\partial T}{\partial t} + \rho \beta \frac{\partial S}{\partial t} \right) dz. \quad (6)$$

172 Inserting (6) into the definition of η_s gives

173
$$\eta_{s} = \int \left[\frac{1}{\bar{\rho}^{z}} \int_{-H}^{0} \rho \alpha \frac{\partial T}{\partial t} \, dz - \frac{1}{\bar{\rho}^{z}} \int_{-H}^{0} \rho \beta \frac{\partial S}{\partial t} \, dz \right] dt, \qquad (7)$$

where the two terms in this expression correspond to the thermosteric and halosteric SSH, respectively. The nonlinear effects of the EOS, which are omitted here, are relatively small. We note that using a linear EOS does not affect the main conclusions of this study, as our goal is to examine the relative importance of the thermosteric and halosteric components rather than to compute their exact magnitudes. As shown in Section 3.3, these two components together accurately reconstruct the total steric SSH.

3 Key results

In this section, we first present a model—data comparison of SSH and ocean circulation in and around the NWES (Section 3.1) to evaluate the model's ability to represent circulation and sea level variability. In Section 3.2, we decompose NWES sea level into different timescales and assess their relative importance. Sections 3.3 and 3.4 quantify the contributions of steric and mass changes to NWES sea level variability, respectively. Finally, Section 3.5 examines the dynamic components of the lateral mass transport and their influence on NWES sea level variability.

3.1 Model-observation comparison: circulation and sea surface height

Since the primary goal of this study is to examine NWES sea level variability, it is essential to validate the model against observational data. To provide a broad view of the large-scale circulation and its variability around the NWES, we first show the time-mean surface geostrophic currents derived from observed mean dynamic topography and from the model SSH in Figures 2a and 2b. The model captures the main currents flowing around the Rockall Trough, Faroe-Shetland Trough, and Norwegian Trench.

Figures 2c and 2d show the surface eddy kinetic energy (EKE) computed from SSH-derived geostrophic velocities for the satellite observations and the model, respectively. Satellite-derived SSH is obtained by optimally interpolating along-track measurements onto a regular 1/8° grid, which filters out many small-scale motions (Chassignet and Xu, 2017). In contrast, the model resolves motions down to its 1/12° resolution. To ensure a fair comparison, the model SSH was filtered with a 10-day temporal and 0.5° spatial window before computing EKE, consistent with Chassignet and Xu (2017), who showed that the altimetry SSH wavenumber spectrum closely matches a 10-day averaged, 150-km spatially filtered model output. The spatial

distribution of EKE is similar between the model and observations, indicating that the model accurately represents variability in surface geostrophic currents. Overall, the model captures both the main currents and their variability around the NWES effectively.

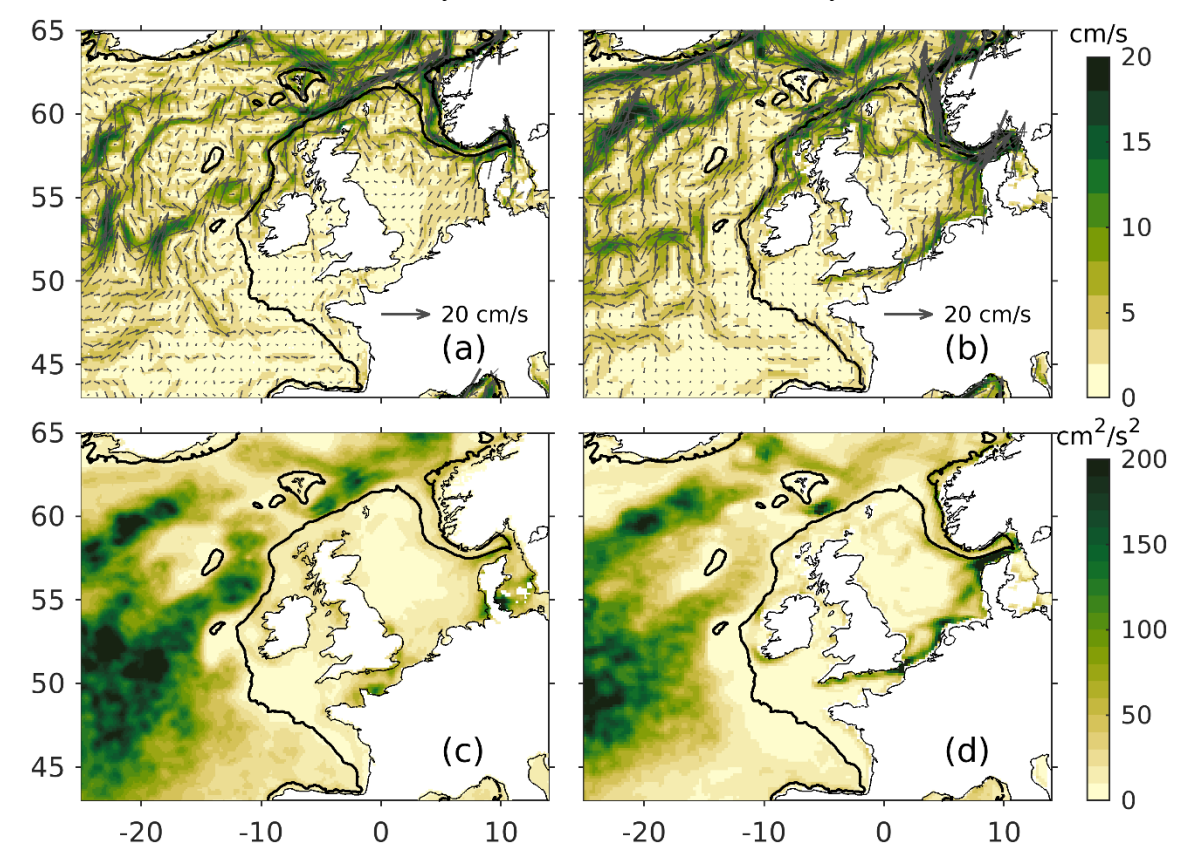


Figure 2. Time-mean surface geostrophic currents (a-b) and surface EKE computed from SSH-derived geostrophic velocities (c-d). (a) Derived from CNES-CLS-2022 Mean Dynamic Topography (MDT). (b) Derived from time-mean model SSH over 2013-2022. (c) Derived from CMEMS (1/8°) over 2013-2022. (d) Derived from model SSH over 2013-2022. Note that the model SSH are 10-day averaged and spatially smoothed with a nominal 0.5° (~60X60 km, 7 X 7 grid points) boxcar window.

We now shift our focus from large-scale circulation to shelf sea level. Modeled SSH is compared with altimetry-derived ADT. Figure 3 shows the monthly SSH anomaly (SSHA) averaged over the NWES for 1993–2022. The model accurately reproduces SSH variability across intraseasonal to interannual timescales. The long-term linear trend in the model SSHA (2.6 cm/decade) is close to the observed trend (3.4 cm/decade), with some differences arising during the final few years of the simulation.

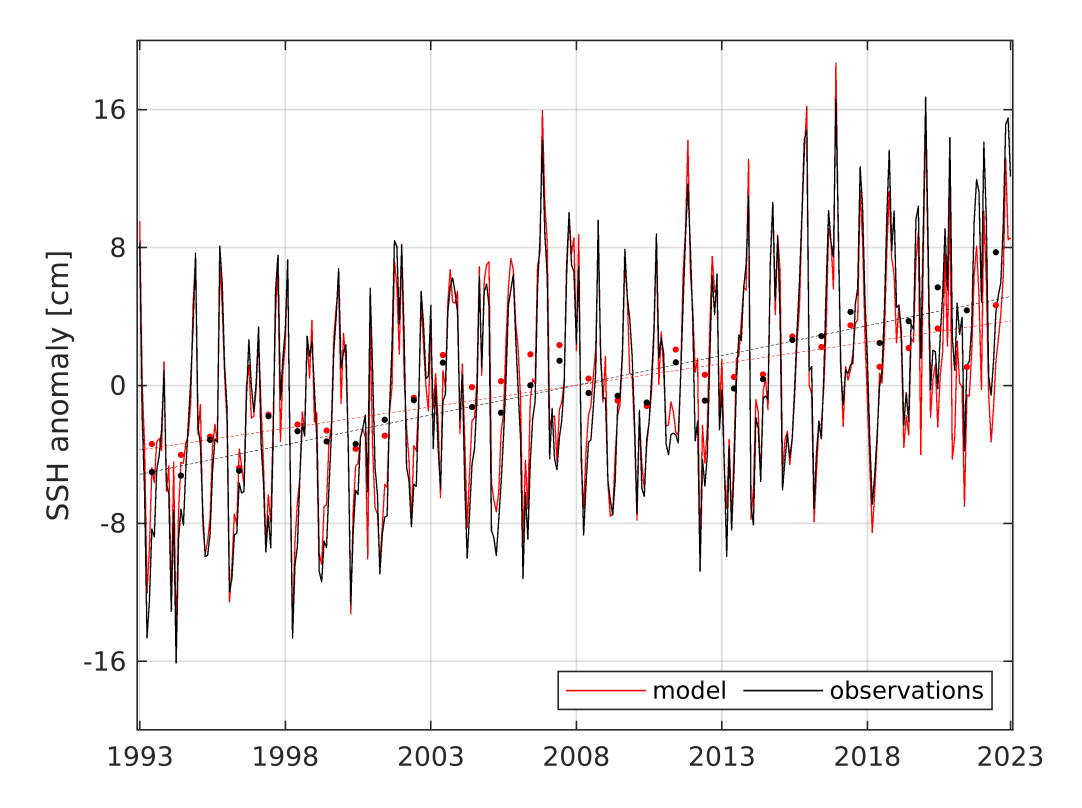


Figure 3. Monthly sea surface heigh anomaly (SSHA) from model and the absolute dynamic topography (ADT) anomaly derived from altimetry observations on the NWES over 1993-2022. Dots denote annual mean values in each year. The anomalies are calculated relative to the 1993-2022 mean. The red (black) dashed lines are the linear trends for the model and observations, respectively.

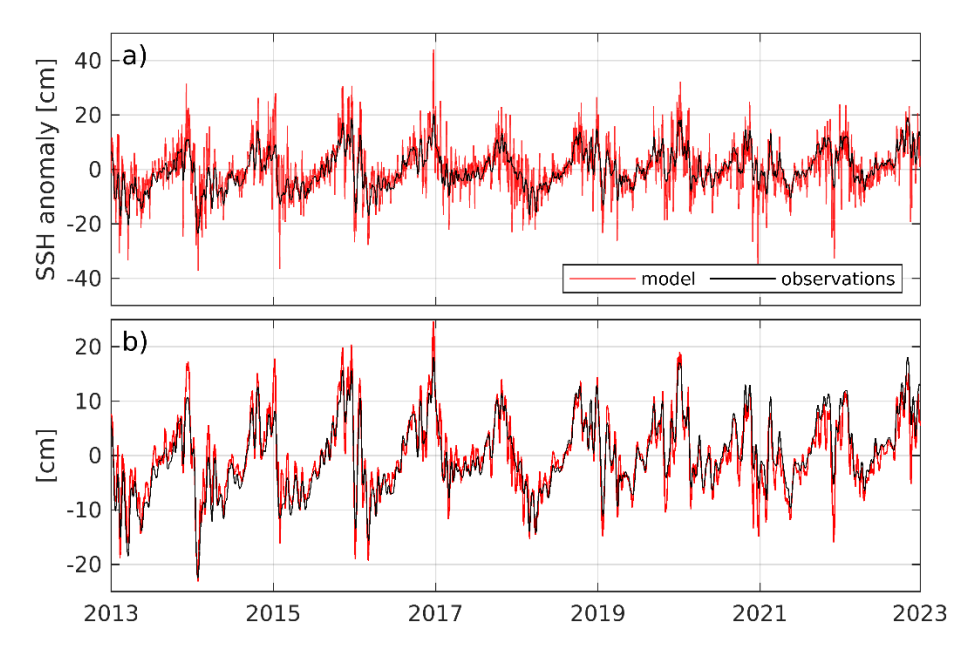


Figure 4. (a) Daily sea surface heigh anomaly (SSHA) from model and the absolute dynamic topography (ADT) anomaly from altimetry observations on the NWES over 2013-2022. (b): ADT anomaly and 10-d average of the SSHA. The anomalies are calculated relative to the 2013-2022 mean. (this is to show the lower SSH variability in observations in panel a) is due to filtering)

To evaluate shorter-timescale variability, we compare daily SSH from the model and observations over 2013–2022 (Figure 4a). The model exhibits larger daily variability than altimetry-derived SSH, reflecting the temporal and spatial smoothing applied to the altimetry data to remove high-frequency fluctuations. To get a fair comparison, we apply a 10-day sliding average to the detrended model SSH. The resulting averaged SSH closely matches altimetry (Figure 4b) with a correlation of 0.93, demonstrating that the model reproduces short-timescale SSH variability accurately.

Since most of our analysis focuses on shelf-averaged NWES SSH, we evaluate whether this metric represents local SSH variability across the shelf. Figure 4 shows the temporal correlation between shelf-averaged and local SSH for both observations and the model. High correlations over most of the shelf confirm that shelf-averaged SSH is a representative measure of local variability.

Overall, the model effectively captures ocean circulation and SSH variability across intraseasonal to interannual timescales on the NWES, supporting its use to investigate NWES SSH variability and its underlying drivers.

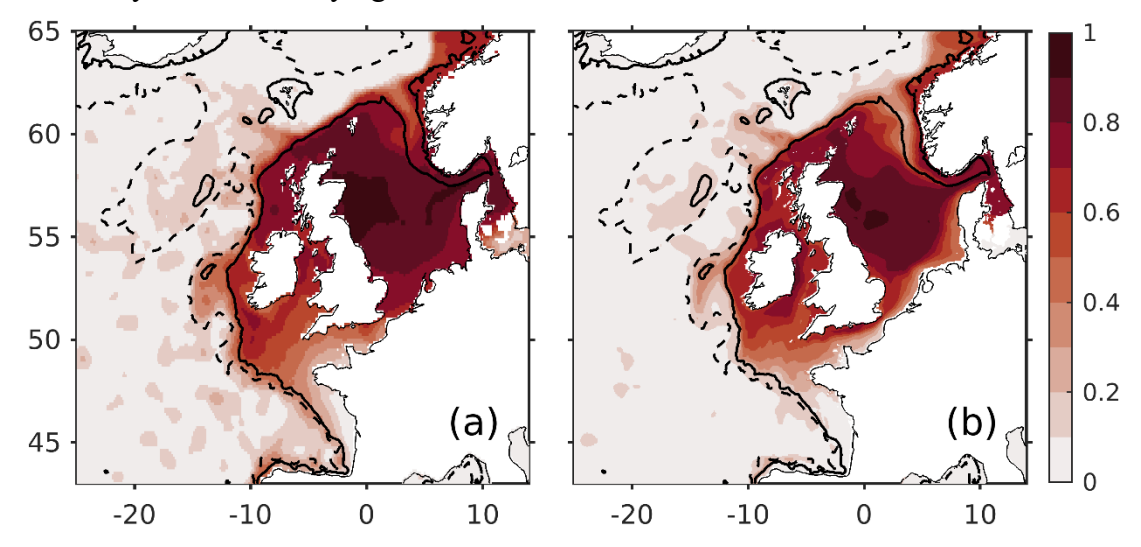


Figure 4. Correlations between the shelf averaged SSH and local SSH for the (a) observations and (b) model. Data are daily from 2013-2022, with linear trends and seasonal cycles removed. The black solid and dashed contour lines denote the 200 m and 1800 m isobaths, respectively.

3.2 SSH variability over different timescales

As noted in the Introduction, a systematic analysis of NWES SSH variability across different timescales is lacking. In this subsection, we decompose SSH variability into four timescales using running-average filters, which are mathematically equivalent to convolutions:

- 1) Interannual variability: computed using a 1-year running average.
- 2) Seasonal cycle: obtained by first calculating the multi-year daily climatology, then applying a 90-day running average.
- 3) Intraseasonal variability (10 90 days): defined as the difference between the 10-day and 90-day running averages.
- 4) High-frequency variability (< 10 days): calculated as the difference between the 10-day running average and the original daily SSH time series.

All analyses use daily model outputs from 2013–2022. Figure 5 shows shelf-averaged SSH time series for each timescale from both the model and observations. The decomposition successfully

separates variabilities, with amplitude increasing as the timescale shortens. The model reproduces NWES SSH well at nearly all timescales, except for the high-frequency component, which is near zero in the observations due to satellite altimetry preprocessing. To quantify their relative contributions, Table 1 lists the temporal standard deviations for each timescale. In the model, the interannual variability accounts for ~17% of total SSH variability (1.4 cm vs. 8.4 cm), whereas seasonal, intraseasonal, and high-frequency components contribute more substantially (e.g., intraseasonal variability is ~50% of total SSH, 4.5 cm vs. 8.4 cm). Observations show similar results, except that the high-frequency component is absent. These results highlight the dominant role of sub-annual variabilities in the NWES sea level, which we further attribute to different physical SSH components in the following sections.

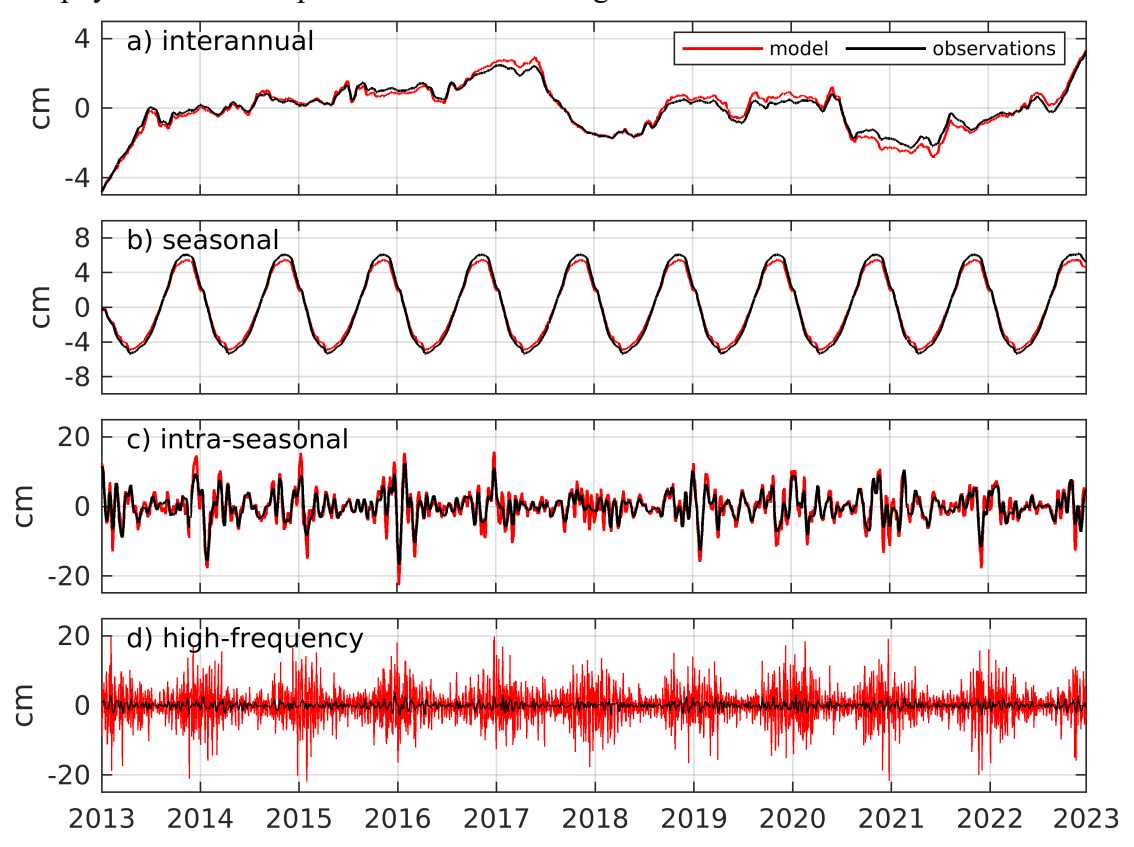


Figure 5. Time series of model and observed shelf averaged SSH decomposed onto different timescales. (a) On the interannual timescale. (b) "Seasonal cycle" of the SSH. (c) On the intraseasonal timescale. (d) On the high-frequency timescale. See text in Section 3.2 for the calculation of these timescales.

Table 1. Variabilities (defined as standard deviations) of the SSH over different timescales from 2013-2022. Values in brackets are estimated from the monthly data over 1993-2022 for comparison. All values are rounded to one decimal place. *This is small because the satellite observed SSH is filtered during pre-processing.

			Timescales		
Standard Deviations of SSH (cm)	All (resolved) timescales	Interannual (1-year average)	Seasonal cycle (90d- average)	Intraseasonal (10d~90d)	High- frequency (< 10d)
Observations	6.5 (5.6)	1.3 (1.4)	4.1	3.7	0.9*
Model	8.4 (5.6)	1.4 (1.8)	3.7	4.5	4.6
Model (η_s)	2.7	0.5	2.4	0.3	0.0
Model (η_m)	7.9	1.5	2.7	4.4	4.5

3.3 Relative contribution of steric to manometric change to the NWES SSH

We now examine the processes contributing to the NWES sea level variability using the time-integrated form of equation (3), which relates directly to SSH rather than its time derivative. In particular, we focus on the effects of mass and steric changes. Daily model outputs of velocity, density, and layer thickness are used to reconstruct the lateral mass flux. While this reconstruction neglects sub-daily correlations between velocity and density, the resulting discrepancy is negligible relative to the variability examined, as indicated by the small residual in the subsequent SSH budget analysis.

Figure 6a shows the different terms of the time-integrated equation averaged over the NWES. As noted previously, the shelf SSH exhibits strong seasonal and intraseasonal variability. The steric SSH (η_s) contributes primarily to the seasonal cycle, accounting for ~17% of total SSH variance. In contrast, the lateral mass flux component (η_m) contributes to both seasonal and intraseasonal variability and explains ~66% of total SSH variance.

Frequency spectra of the three terms (Figure 6b) show a close correspondence between total SSH and η_m . The power of η_s is at least an order of magnitude weaker than that of SSH and η_m , except at the annual (1-year) period corresponding to the seasonal cycle. At timescales shorter than ~50 days (frequency > 2 × 10⁻² day⁻¹), the spectrum of η_s decays more rapidly,

indicating reduced variability at high frequencies. Table 1 summarizes contributions of each timescale to η_s and η_m . The variability in η_s is dominated by the seasonal cycle, with other timescales playing only a minor role. In contrast, η_m exhibits substantial contributions from seasonal, intraseasonal, and high-frequency variability, all of which are important to the total η_m .

The seasonal cycles from η_s and η_m are comparable to each other, highlighting the importance of both components in driving the seasonal SSH variability. The interannual variability of the total SSH is mainly driven by η_m , as its variance exceeds that of η_s on this timescale. Overall, the NWES SSH variability -- from high-frequency through intraseasonal to interannual timescales -- is primarily controlled by mass changes rather than density variations. This finding is consistent with, and extends, previous studies (e.g., Wise et al., 2024; Diabaté et al., 2025).

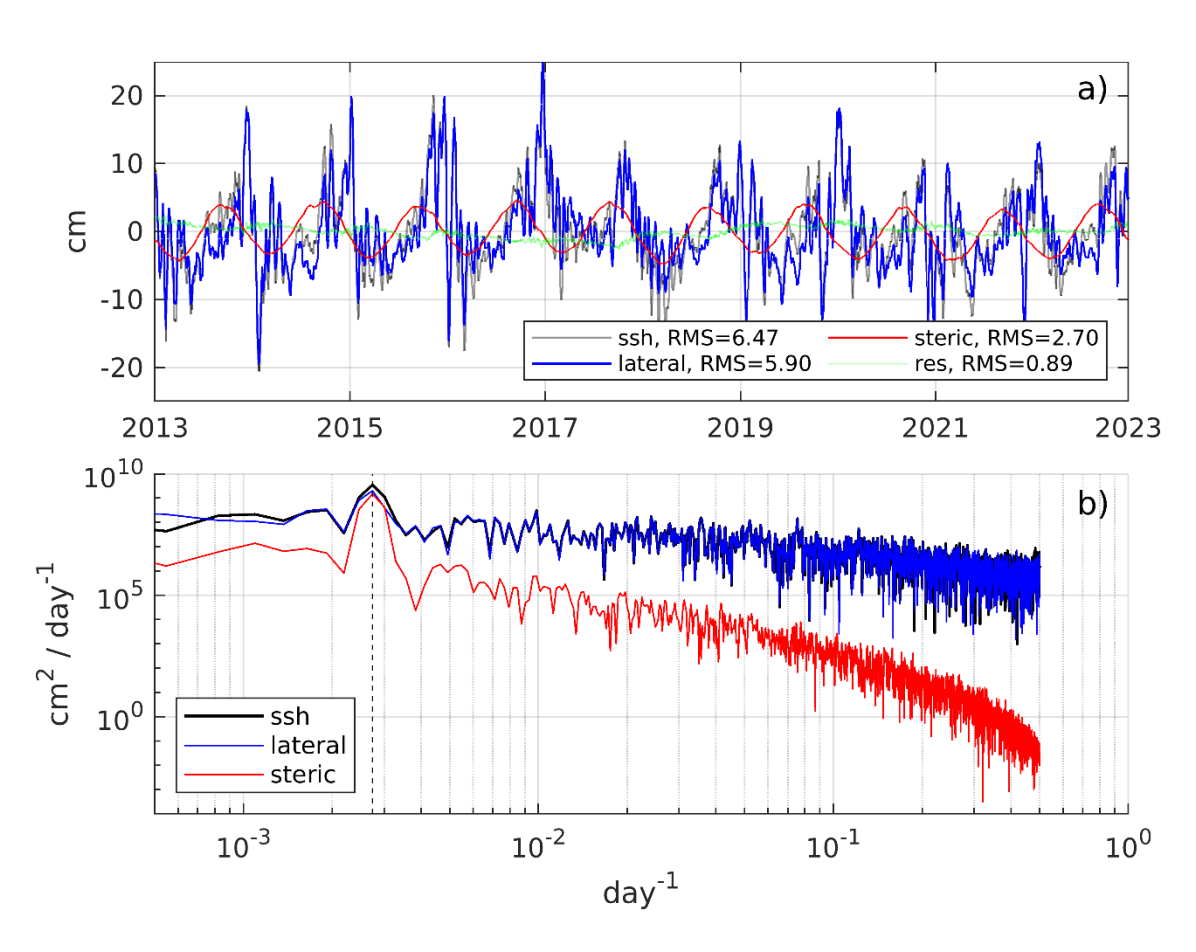


Figure 6. (a) Time evolution of the terms in the time integrated SSH budget averaged over the European Shelf (denoted by the dotted area in Figure 1). Grey line is SSH anomaly relative to the

314	initial value, blue is the contribution of lateral mass flux to SSH (η_m) , red is the steric SSH (η_s) .
315	green is residual. Daily data are used, and the terms are 10-d averaged. Linear trends are
316	removed for all terms. (b) Power density spectrum for the original SSH anomaly, η_l and η_s .
317	Vertical dashed line denotes period of 1 year.

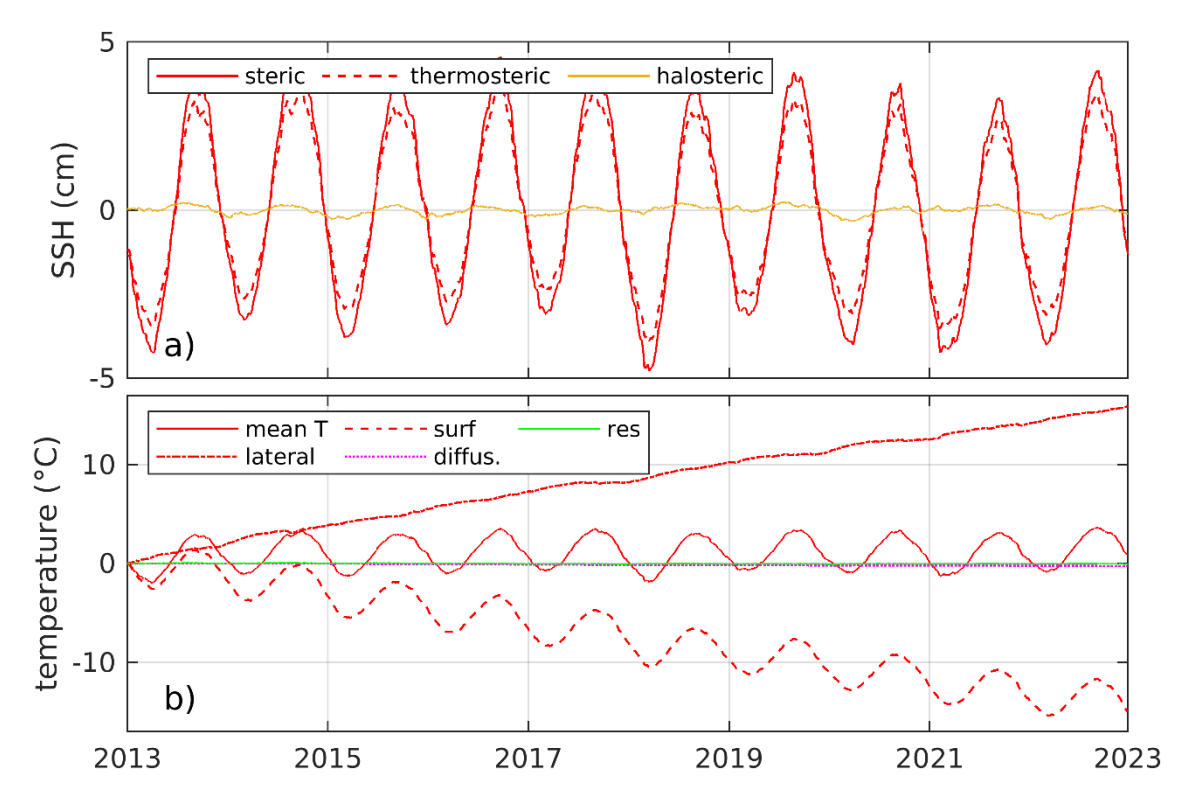


Figure 7. (a) Partitioning of the steric SSH change (red solid line) into the thermosteric (dashed line) and halosteric (orange solid line) components. Linear trends are removed for all series. (b) Time evolution of the terms in the time-integrated thermal equation (5) averaged over the shelf region. All terms are normalized by the ocean depth in the NWES to have the unit of temperature [°C]. Solid line is the mean temperature change, dashed-dotted line is the contribution of lateral heat flux, dashed line is the contribution of surface heat flux, magenta dotted line is the heat diffusion, green line is residual due to numerical errors. Note that the red solid line in (b) is essentially proportional to the thermosteric SSH (red dashed line in a)).

We first focus on the steric component of SSH. To assess the effects of temperature and salinity, steric SSH is separated into thermosteric and halosteric components using equation (7). Figure 7a shows their time series. The steric SSH variability is clearly dominated by the thermosteric component, while the halosteric component contributes only a minor linear trend (removed here). Thus, the seasonal variation of steric SSH over the NWES is primarily driven by regional temperature changes rather than salinity. The small residual between steric SSH and the

sum of thermosteric and halosteric components may arise from the use of a linear equation of state.

To further explore processes controlling the thermosteric change, we use the column-integrated thermal equation in HYCOM (Bleck, 2002):

338
$$\sum_{k} \partial_{t}(T_{k}h_{k}) = -\sum_{k} \nabla \cdot (\mathbf{u}_{k}h_{k}T_{k}) + \frac{F_{surf}}{\rho c_{p}} + \sum_{k} \nabla \cdot (\kappa h_{k} \nabla T_{k}), \quad (8)$$

where "k" denotes layer number, T is temperature, h is layer thickness, F_{surf} is the surface heat flux into the ocean (W m⁻²), ρ is seawater density, c_p is specific heat capacity of seawater (J (kg K)⁻¹), and κ is heat diffusivity (m² s⁻¹). The left-hand side is proportional to the thermosteric SSH change. The first two terms on the right-hand side represent lateral and surface heat fluxes, while the last term represents subgrid-scale heat diffusion, which is small relative to the other terms. Integrating equation (8) spatially over the NWES and dividing by the ocean volume gives the rate of mean temperature change on the shelf. Figure 7b shows the time-integrated contributions. The temperature evolution term (solid line) exhibits seasonal variability closely matching the thermosteric SSH. Surface heat fluxes (dashed line) drive both seasonal variability and a net cooling, while lateral heat transport primarily causes a net warming without significant variability.

In summary, the steric change contributes to NWES SSH variability mainly on seasonal timescale, dominated by temperature rather than salinity changes. Seasonal variation in surface heating and cooling is the primary driver of this thermosteric SSH variability.

3.4 Contribution of mass change to the NWES SSH

As shown above, the dominant component of the NWES SSH is the lateral mass flux convergence (the manometric component η_m), which explains most of the total SSH variability and exhibits multiscale variations from seasonal to high-frequency (Table 1). Notably, the seasonal cycle of η_m is comparable in magnitude to that of steric SSH, indicating that seasonal variations in total SSH are influenced not only by surface heating and cooling but also by seasonality in lateral ocean processes, such as circulation and wind around the shelf. In this section, we investigate the drivers of η_m across different timescales.

Given the complexity of the NWES circulation and the dominant role of wind forcing, we first examine the relationship between regional wind and η_m (blue line in Figure 6a). Figure 8 shows correlation coefficients between the two fields. η_m is highly correlated with the zonal wind stress at the northern boundary, reflecting meridional Ekman transport that drives mass variations on the NWES and the corresponding SSH changes. Similarly, high correlations between η_m and meridional wind stress are observed along the western boundary, consistent with zonal Ekman transport. These results indicate that the lateral mass flux into the shelf is primarily driven by wind-induced transport, in agreement with previous studies (e.g., Wise et al., 2024).

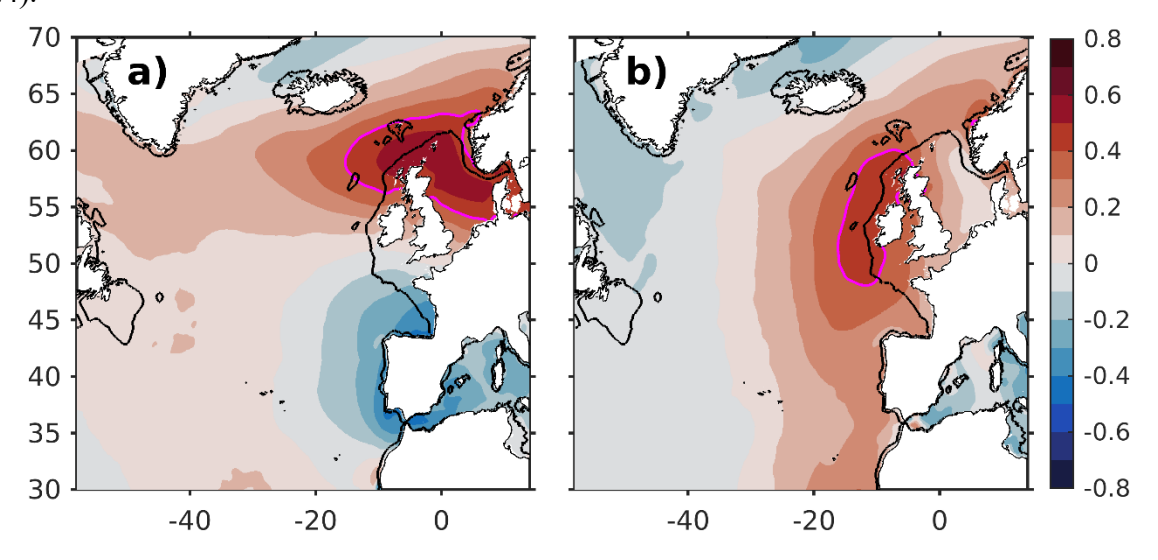


Figure 8. Correlations between the lateral flux contribution to the shelf SSH (η_m) and the local wind stresses over 2013-2022: (a) for the zonal wind stress and (b) for the meridional wind stress. Magenta line denotes the contour line of 0.4 for the correlation coefficient; black line is the 200m isobath.

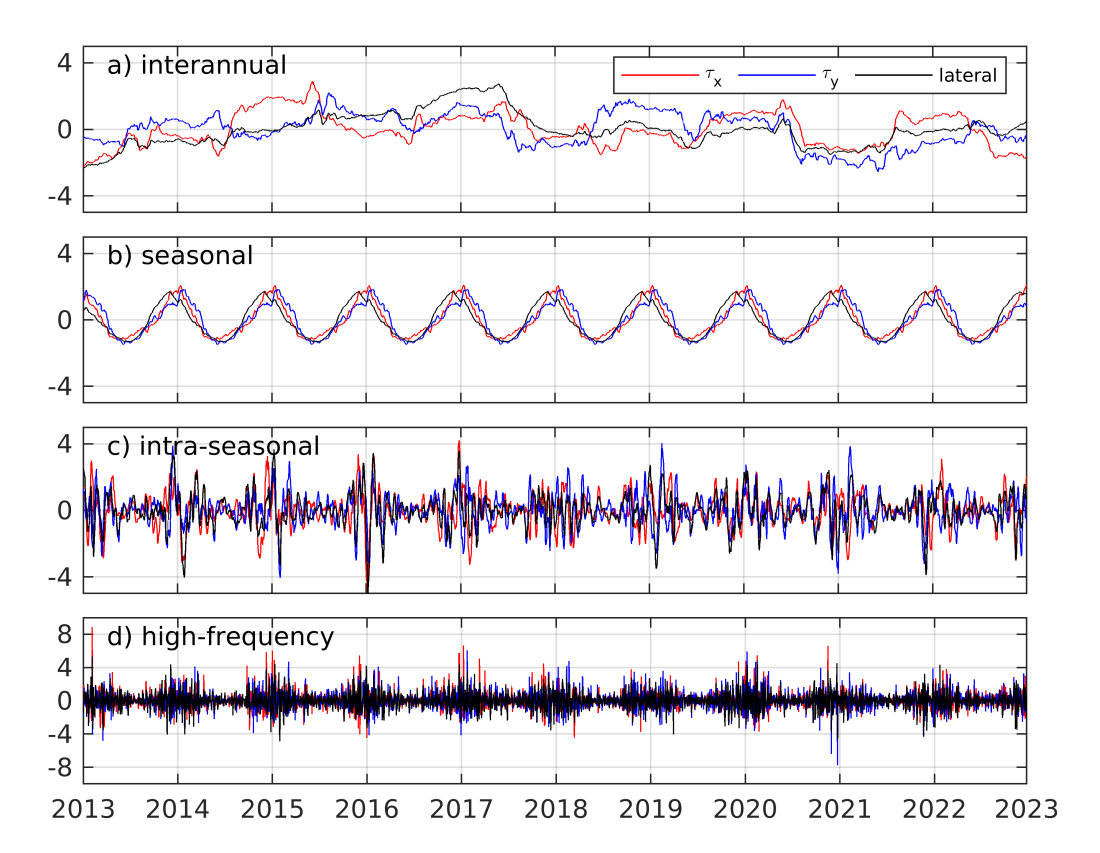


Figure 9. Time series of wind stress averaged in the region of high correlation (magenta lines in Figure 8) and the lateral term over different timescales. (a) Time series on the interannual timescale. (b) Time series on the seasonal timescale. (c) Time series on the intraseasonal timescale. (d) Time series on the high-frequency timescale. All series are normalized by their respective standard deviations.

To examine this relationship across timescales, local wind stresses are decomposed into the same four timescales as η_m and correlated with the corresponding η_m components. Figure 9 shows time series of normalized η_m and wind stresses averaged over areas where correlation exceeds 0.4. We see that η_m covaries with wind stresses over all four timescales, wind stresses across all four timescales, highlighting the importance of wind in driving lateral mass flux convergence into the shelf.

Figure 10 shows the spatial patterns of correlations between η_m and wind stress at each timescale. On intraseasonal and high-frequency scales, the patterns resemble those of the full timescale (Figure 8), with strong correlations between zonal (meridional) wind at the northern (western) boundary and η_m . The correlations on seasonal scale are even stronger, reflecting the dominant role of seasonally varying wind in driving mass changes on the shelf. At interannual timescale, high correlations extend to broader regions, including the Labrador Sea, suggesting a link between large-scale atmospheric variability and lateral mass flux convergence, which warrants further investigation using longer model simulations. Correlations at high-frequency timescale are weaker but still statistically significant, likely due to short-scale motions not directly driven by wind.

In summary, the lateral mass flux contribution to NWES SSH is closely linked to regional wind via the Ekman transport mechanism (Hermans et al., 2022). This relationship holds across interannual, seasonal, intraseasonal, and high-frequency timescales, although the spatial patterns of the correlation vary depending on the timescale.

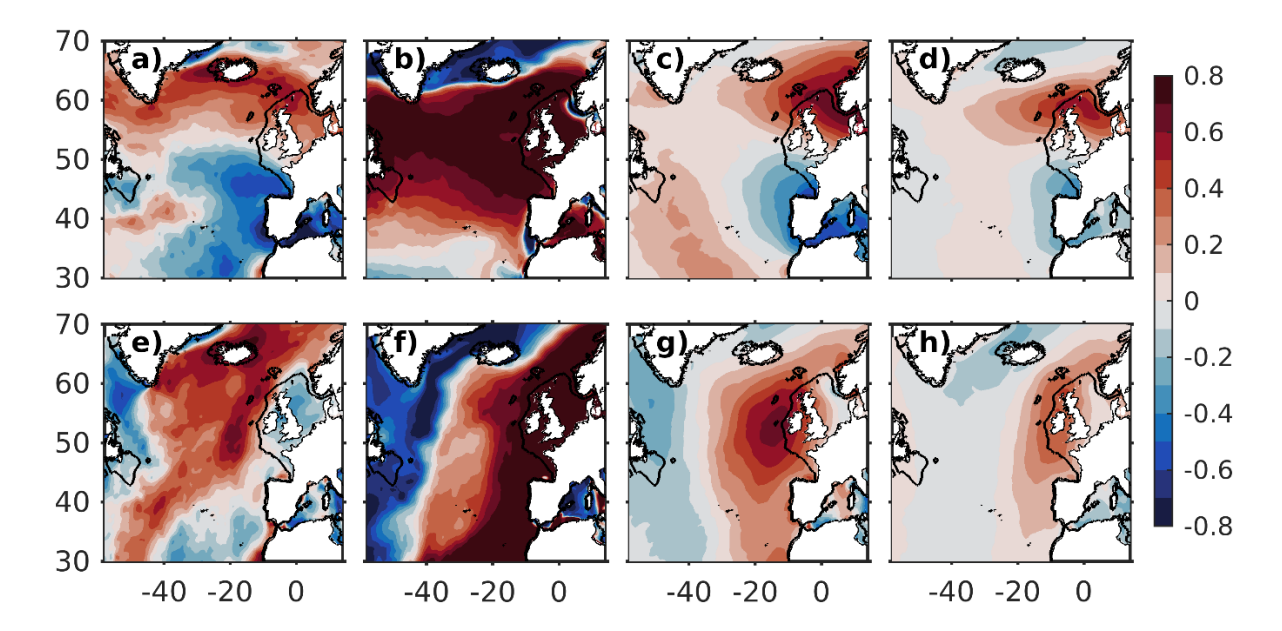


Figure 10. Correlations between the lateral mass flux contribution to the shelf SSH (η_m) and the local wind stresses over different timescales. (a-d) For zonal wind stress; (e-h) for meridional wind stress. (a, e) On the interannual timescale. (b, f) On the seasonal timescale. (c, g) On the intraseasonal timescale. (d, h) On the high-frequency timescale. Correlations on land points are masked out.

3.5 Decomposition of the lateral mass transport

In the previous section, we established the link between regional wind stress and the mass contribution to shelf SSH, consistent with prior studies. However, this relationship is somewhat surprising because SSH or mass/volume changes in a region are directly determined by the time-integrated mass transport into the region, whereas wind stress is proportional to the instantaneous Ekman transport rather than its integral.

To further examine the contribution of lateral mass transport to shelf SSH, we decompose the transport into different dynamic components, including the Ekman transport. This decomposition approach, previously employed by Wise et al. (2024) under a Boussinesq framework to study volumetric flow across the European shelf, is here applied in a non-Boussinesq framework to the mass flux convergence in equation (2):

$$-\frac{\nabla \cdot \mathbf{U}^{\rho}}{\bar{\rho}^{z}} = -\frac{\nabla \cdot \mathbf{U}^{\rho}_{geo}}{\bar{\rho}^{z}} - \frac{\nabla \cdot \mathbf{U}^{\rho}_{Eks}}{\bar{\rho}^{z}} - \frac{\nabla \cdot \mathbf{U}^{\rho}_{Ekb}}{\bar{\rho}^{z}} + res. \quad (9)$$

Here, \mathbf{U}_{geo}^{ρ} is the lateral mass flux associated with the geostrophic current and is calculated from pressure gradients:

$$\mathbf{U}_{geo}^{\rho} = \int_{-H}^{0} \frac{\hat{\mathbf{k}} \times \nabla p}{f} \, \mathrm{d}z,$$

 \mathbf{U}_{Eks}^{ρ} and \mathbf{U}_{Ekb}^{ρ} are the lateral mass flux convergences due to the surface and bottom Ekman currents, respectively:

$$\mathbf{U}_{Eks}^{\rho} = -\frac{\hat{\mathbf{k}} \times \boldsymbol{\tau}^{s}}{f}, \quad \mathbf{U}_{Ekb}^{\rho} = -\frac{\hat{\mathbf{k}} \times \boldsymbol{\tau}^{b}}{f},$$

where τ^s is wind stress [N m⁻²]. The bottom stress τ^b is calculated as

$$\boldsymbol{\tau}^b = C_d(|\mathbf{u}_b| + \mathbf{u}_*)\mathbf{u}_b,$$

where $C_d = 1 \times 10^{-3}$ is quadratic bottom drag coefficient, $u_* = 0.05 \, m/s$ is the rms flow speed used for linear bottom friction, and \mathbf{u}_b is the near-bottom velocity in the bottom boundary layer (10 m in our model). The residual (res.) term accounts for unrepresented processes, such as the kinetic energy gradient term in the momentum equation. These are less significant than the geostrophic and Ekman terms (Wise et al., 2024) in the total mass transport and are therefore neglected here. Although we work with mass flux, the units of all terms in equation (9) are equivalent to volume flux (Sv), since mass fluxes are normalized by the column-mean density.

All terms in equation (9) are integrated over the NWES at each time step. Using the divergence theorem, the resulting terms represent the net mass (or volume) transport into the shelf. Figure 11a shows the original and 10-day averaged time series of the total, geostrophic, and summed Ekman (surface plus bottom) transports from 2013–2022. The geostrophic and Ekman transports covary inversely (r = -0.94 for the original series), indicating a near balance between them. The total transport, representing the residual of the geostrophic and Ekman components, is an order of magnitude smaller than either component. The surface Ekman transport dominates over the bottom component (standard deviations: 2.9 Sv vs. 0.4 Sv), highlighting the importance of wind in the lateral transport across the shelf. Figures 11b and 11c show scatter plots of the geostrophic versus summed Ekman transports for the original and 10-day averaged series, respectively, illustrating that geostrophic and Ekman transports largely compensate each other. This compensation occurs because the wind-driven Ekman transport

accumulates or removes water from the shelf, inducing pressure gradients that drive a geostrophic response opposite to the Ekman transport. Consequently, the net lateral mass transport into the NWES is primarily determined by the balance between wind-driven Ekman transport and geostrophic adjustment.

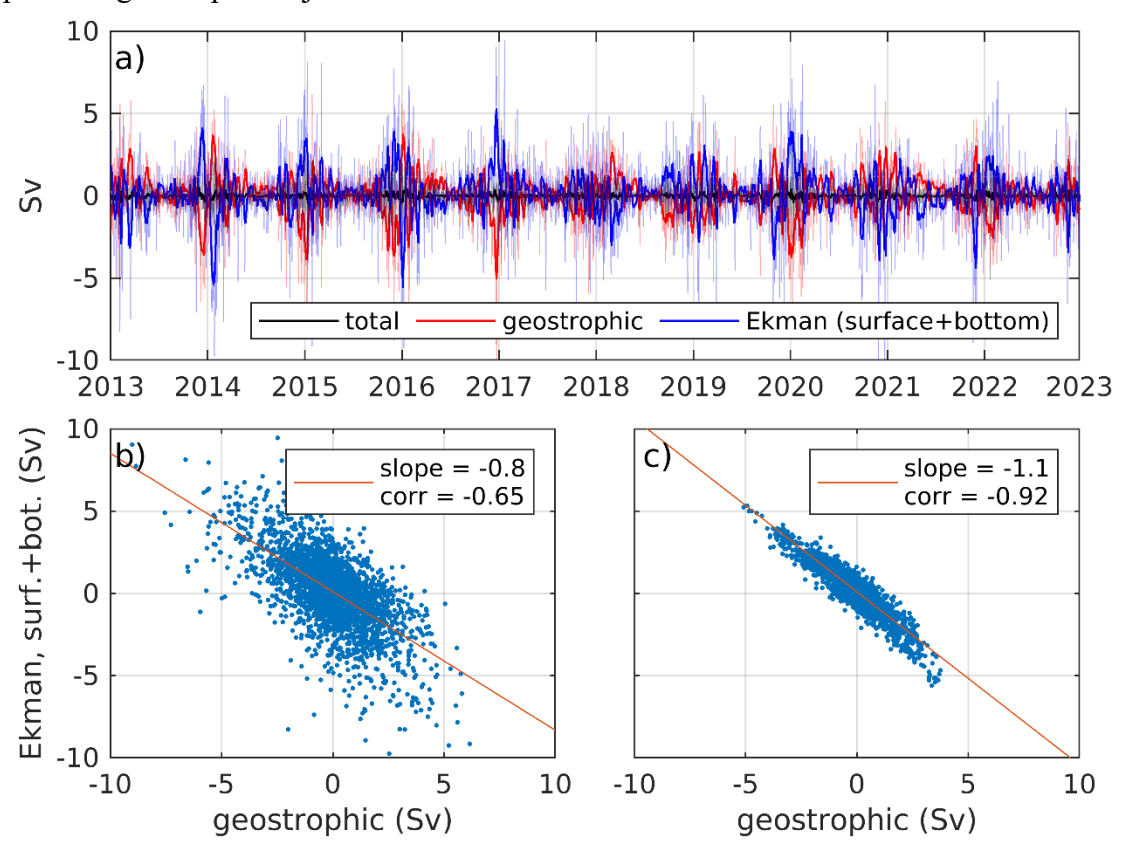


Figure 11. Decomposition of the total lateral mass flux into the shelf region. (a) Time series of the total flux (black), the geostrophic transport (red), and the sum of the surface and bottom Ekman transport (blue). Thick lines are original daily time series, and transparent lines are 10-d averages. (b) Scatter plot of the original geostrophic and summed Ekman transports over 2013-2022. (c) Same as (b) but for the 10-d averaged time series. Red line is a linear fit. All mass fluxes are normalized by vertically averaged density and the units are Sv.

4 Conclusions and discussion

In this study, we examined the sea level variability on the Northwest European Shelf (NWES) and its drivers across interannual, seasonal, intraseasonal, and high-frequency (<10 days) timescales. Using outputs from a realistic Atlantic Ocean simulation and the kinematic evolution equation of sea surface height (SSH), we find that the model captures NWES SSH

variability well across all timescales, as well as the long-term trend. The SSH variability is decomposed into components arising from local steric (density) changes and mass changes. Our main findings are as follows:

- The NWES SSH variability is comparably high at high-frequency, intraseasonal, and seasonal timescales (4.6, 4.5, and 3.7 cm, respectively; Table 1), while interannual variability is smaller (1.4 cm), representing roughly 17% of the total variability (8.4 cm).
- The steric and mass changes account for ~17% and ~66% of total NWES SSH variability, respectively. The steric variability occurs primarily at seasonal timescale and is dominated by temperature rather than salinity changes. Seasonal surface heat flux drives this temperature variation, while lateral heat transport contributes to a net warming with limited temporal variability.
- The lateral mass transport contributes to SSH variability across all timescales. It dominates intraseasonal and high-frequency variability and exceeds the steric effect at seasonal and interannual scales. The manometric SSH component is strongly correlated with regional wind stress across all timescales (except for interannual scale where remote wind also plays a role), reflecting wind-driven Ekman transport. The net lateral mass transport onto the shelf, driven by surface winds, induces pressure gradient responses and geostrophic currents that largely compensate the Ekman flux.

Overall, mass changes due to lateral transport play a more significant role in NWES SSH variability than steric changes. This is consistent with observations in other shelf regions, where cross-shelf mass transport dominates near-coast sea level variability (Vinogradova et al., 2007; Steinberg et al., 2024). In contrast, steric changes are often the main driver of long-term SSH variability in the open ocean (Landerer et al., 2007; Yin et al., 2010). Importantly, short-term SSH variability on the NWES exhibits larger magnitudes than interannual or longer-term timescales, highlighting the importance of high-frequency processes. While the long-term warming trends remain crucial, they may amplify short-term variability, as suggested by studies on extreme sea levels (Tebaldi et al., 2021) and marine heatwaves (Frölicher et al., 2018).

The seasonality in both the steric and mass components underscores the dual role of seasonal solar radiation: surface heating and cooling induce a seasonal steric SSH signal, while

seasonally varying wind stress enhances the accumulation and discharge of water on the shelf, driving seasonal variability in the manometric SSH.

The strong influence of wind on mass changes across all timescales highlights the importance of atmospheric conditions in shaping NWES sea level. While the link between large-scale atmospheric patterns and interannual SSH variability is well established (Calafat et al., 2012; Chafik et al., 2017), shorter timescales and spatial patterns are less understood. This study provides a comprehensive framework to quantify wind-driven contributions to NWES sea level variability.

Finally, the wind is not the only driver of the sea level variability. The wind-driven Ekman transport is partially compensated by geostrophic currents, which are also influenced by large- and meso-scale ocean dynamics and Earth's rotation. These slowly-evolving currents can affect the lateral transport and, thus, shelf sea level on longer timescales. Their role in regional sea level changes warrants further investigation.

Acknowledgments:

491

492

493

494

495

496

497

498

499

500

501

502

503

504

515

520

- 505 YL, XX, and EPC acknowledge support from the National Science Foundation (NSF) under
- grant OCE-2349841, funded through the joint UK–US Climate Consequences of Rapid Ocean
- 507 Changes (CCROC) program. The high-resolution HYCOM simulations were carried out on
- 508 supercomputers at the U.S. Army Engineer Research and Development Center in Vicksburg,
- Mississippi, using computing time provided by the U.S. Department of Defense High
- Performance Computing Modernization Program. We also acknowledge the high-performance
- 511 computing support from Derecho (https://doi.org/10.5065/qx9apg09) provided by NCAR's
- 512 Computational and Information Systems Laboratory sponsored by the NSF. The authors also
- 513 thank Drs. Neil Fraser (SAMS/UK) and Anthony Wise (NOC/UK) for their constructive
- 514 discussions that contributed to this work.

Data Availability Statement:

- The source code of the HYCOM model can be found at: https://github.com/HYCOM/HYCOM-
- 517 <u>src</u>. The CMEMS sea level anomaly data can be found at: https://doi.org/10.48670/moi-00149.
- The analysis codes for this study are available at: https://doi.org/10.5281/zenodo.17281677. The
- 519 processed data are available at: https://doi.org/10.5281/zenodo.17281693.

References:

- Beckley, B. D., Callahan, P. S., Hancock, D. W., Mitchum, G. T., & Ray, R. D. (2017). On the
- "cal-mode" correction to TOPEX satellite altimetry and its effect on the global mean sea level
- time series. Journal of Geophysical Research: Oceans, 122(11), 8371–8384.
- 524 https://doi.org/10.1002/2017JC013090
- Bleck, R. (2002). An oceanic general circulation model framed in hybrid isopycnic-Cartesian
- 526 coordinates. Ocean modelling, 4(1), 55-88.
- 527 Calafat, F. M., Chambers, D. P., & Tsimplis, M. N. (2012). Mechanisms of decadal sea level
- variability in the eastern North Atlantic and the Mediterranean Sea. Journal of Geophysical
- 529 Research: Oceans, 117(C9).
- 530 Chafik, L., Nilsen, J. E. Ø., & Dangendorf, S. (2017). Impact of North Atlantic teleconnection
- patterns on Northern European sea level. Journal of Marine Science and Engineering, 5(3), 43.
- Chassignet, E. P., Smith, L. T., Halliwell, G. R., & Bleck, R. (2003). North Atlantic simulations
- with the Hybrid Coordinate Ocean Model (HYCOM): Impact of the vertical coordinate choice,
- reference pressure, and thermobaricity. Journal of Physical Oceanography, 33(12), 2504-2526.
- Chassignet, E. P., & Xu, X. (2017). Impact of horizontal resolution (1/12 to 1/50) on Gulf Stream
- separation, penetration, and variability. Journal of Physical Oceanography, 47(8), 1999-2021.
- Church, J. A., and White, N. J. (2011). Sea-Level Rise from the Late 19th to the Early 21st
- 538 Century. Surveys in Geophysics, 32(4-5), 585–602. http://doi.org/10.1007/s10712-011-9119-1
- 539 CMEMS. (2024a). SEALEVEL GLO PHY L4 NRT 008 046 [Dataset]. E.U. Copernicus
- Marine Service Information (CMEMS). Marine Data Store (MDS).
- 541 https://doi.org/10.48670/moi-00149
- 542 CMEMS. (2024b). SEALEVEL GLO PHY MDT 008 063 [Dataset]. E.U. Copernicus Marine
- Service Information (CMEMS). Marine Data Store (MDS). https://doi.org/10.48670/moi-
- 544 00150
- Dangendorf, S., Calafat, F. M., Arns, A., Wahl, T., Haigh, I. D., & Jensen, J. (2014). Mean sea
- level variability in the North Sea: Processes and implications. Journal of Geophysical Research:
- 547 Oceans, 119(10).

- Diabaté, S. T., Fraser, N. J., White, M., Berx, B., Marié, L., & McCarthy, G. D. (2025). On the
- wind-driven European shelf sea-level variability and the associated oceanic circulation.
- 550 Continental Shelf Research, 291, 105466.
- Dorandeu, J., & Le Traon, P. Y. (1999). Effects of global mean atmospheric pressure variations
- on mean sea level changes from TOPEX/Poseidon. Journal of Atmospheric and Oceanic
- 553 Technology, 16(9), 1279-1283.
- Fraser, N. J., Cunningham, S. A., Drysdale, L. A., Inall, M. E., Johnson, C., Jones, S. C., ... &
- Holliday, N. P. (2022). North Atlantic Current and European slope current circulation in the
- Rockall Trough observed using moorings and gliders. Journal of Geophysical Research: Oceans,
- 557 127(12), e2022JC019291.
- Frederikse, T., Landerer, F., Caron, L. et al. The causes of sea-level rise since 1900. Nature 584,
- 559 393–397 (2020). https://doi.org/10.1038/s41586-020-2591-3
- 560 Gregory JM, Griffies SM, Hughes CW, Lowe JA, Church JA, Fukimori I, Gomez N, Kopp RE,
- Landerer F, Le Cozannet G, Ponte RM, Stammer D, Tamisiea ME, van de Wal RSW (2019)
- Concepts and terminology for sea level: mean variability and change, both local and global. Surv
- 563 Geophys 9:9–10. https://doi.org/10.1007/s10712-019-09525-z
- Griffies, S. M., & Greatbatch, R. J. (2012). Physical processes that impact the evolution of global
- mean sea level in ocean climate models. Ocean Modelling, 51, 37-72.
- 566 Gill, A. E., & Niller, P. P. (1973, February). The theory of the seasonal variability in the ocean. In
- Deep Sea Research and Oceanographic Abstracts (Vol. 20, No. 2, pp. 141-177). Elsevier.
- Halliwell, G. R. (2004). Evaluation of vertical coordinate and vertical mixing algorithms in the
- 569 HYbrid-Coordinate Ocean Model (HYCOM). Ocean Modelling, 7(3-4), 285-322.
- Hamlington BD, Bellas-Manley A, Willis JK, et al. (2024). The rate of global sea level rise
- doubled during the past three decades. Communications Earth & Environment.; 5: 601. doi:
- 572 10.1038/s43247-024-01761-5
- Hansen, B., & Østerhus, S. (2000). North atlantic-nordic seas exchanges. Progress in
- 574 oceanography, 45(2), 109-208.

- Hermans, T. H., Le Bars, D., Katsman, C. A., Camargo, C. M., Gerkema, T., Calafat, F. M., ... &
- 576 Slangen, A. B. (2020). Drivers of interannual sea level variability on the northwestern European
- shelf. Journal of Geophysical Research: Oceans, 125(10), e2020JC016325.
- Holt, J., Wakelin, S., Lowe, J., & Tinker, J. (2010). The potential impacts of climate change on
- 579 the hydrography of the northwest European continental shelf. Progress in Oceanography, 86(3-
- 580 4), 361-379.
- Houpert, L., Cunningham, S., Fraser, N., Johnson, C., Holliday, N. P., Jones, S., ... & Rayner, D.
- 582 (2020). Observed variability of the North Atlantic Current in the Rockall Trough from 4 years of
- mooring measurements. Journal of Geophysical Research: Oceans, 125(10), e2020JC016403.
- Huthnance, J., Hopkins, J., Berx, B., Dale, A., Holt, J., Hosegood, P., ... & Spingys, C. (2022).
- Ocean shelf exchange, NW European shelf seas: Measurements, estimates and comparisons.
- Progress in Oceanography, 202, 102760.
- Jousset S., Mulet S., Wilkin J., Greiner E., Dibarboure G. and Picot N.: "New global Mean
- 588 Dynamic Topography CNES-CLS-22 combining drifters, hydrological profiles and High
- 589 Frequency radar data", OSTST 2022, https://doi.org/10.24400/527896/a03-2022.3292.
- Landerer, F. W., Jungclaus, J. H., & Marotzke, J. (2007). Regional dynamic and steric sea level
- change in response to the IPCC-A1B scenario. Journal of Physical Oceanography, 37(2), 296-
- 592 312.
- 593 Lu, Y., Zhai, L., Hu, X., Horwitz, R., Paquin, J. P., Hannah, C., & Crawford, W. (2025). Sea
- Level Variations in Shelf Waters off the Coast of British Columbia: From Subsynoptic to
- 595 Interannual Time Scales. Journal of Physical Oceanography, 55(1), 59-74.
- 596 McDougall, T. J., & Barker, P. M. Getting started with TEOS-10 and the Gibbs Seawater (GSW)
- 597 Oceanographic Toolbox. SCOR/ IAPSO WG127 (2011).
- Melet, A., van de Wal, R., Amores, A., Arns, A., Chaigneau, A. A., Dinu, I., Haigh, I. D.,
- Hermans, T. H. J., Lionello, P., Marcos, M., Meier, H. E. M., Meyssignac, B., Palmer, M. D.,
- Reese, R., Simpson, M. J. R., and Slangen, A. B. A.: Sea Level Rise in Europe: Observations and
- projections, in: Sea Level Rise in Europe: 1st Assessment Report of the Knowledge Hub on Sea
- Level Rise (SLRE1), edited by: van den Hurk, B., Pinardi, N., Kiefer, T., Larkin, K.,
- Manderscheid, P., and Richter, K., Copernicus Publications, State Planet, 3-slre1, 4,
- 604 https://doi.org/10.5194/sp-3-slre1-4-2024, 2024.

- Nicholls, R. J., & Cazenave, A. (2010). Sea-level rise and its impact on coastal zones. Science,
- 606 328(5985), 1517-1520.
- Piecuch, C. G., Thompson, P. R., Ponte, R. M., Merrifield, M. A., & Hamlington, B. D. (2019).
- What caused recent shifts in tropical Pacific decadal sea-level trends?. Journal of Geophysical
- 609 Research: Oceans, 124. https://doi.org/10.1029/2019JC015339
- Piecuch, C. G., Fukumori, I., Ponte, R. M., Schindelegger, M., Wang, O., & Zhao, M. (2022).
- 611 Low-frequency dynamic ocean response to barometric-pressure loading. *Journal of Physical*
- 612 *Oceanography*, 52(11), 2627-2641.
- Rosmond, T.E., J. Teixeira, M. Peng, T.F. Hogan, and R. Pauley. 2002. Navy Operational Global
- Atmospheric Prediction System (NOGAPS): Forcing for ocean models. Oceanography 15(1):99–
- 615 108, http://dx.doi.org/10.5670/oceanog.2002.40.
- 616 Saha, S., Moorthi, S., Pan, H. L., Wu, X., Wang, J., Nadiga, S., ... & Goldberg, M. (2010). The
- NCEP climate forecast system reanalysis. Bulletin of the American Meteorological Society,
- 618 91(8), 1015-1058.
- Savage, A. C., Arbic, B. K., Alford, M. H., Ansong, J. K., Farrar, J. T., Menemenlis, D., ... &
- 620 Zamudio, L. (2017). Spectral decomposition of internal gravity wave sea surface height in global
- models. Journal of Geophysical Research: Oceans, 122(10), 7803-7821.
- 622 Steinberg, J. M., Griffies, S. M., Krasting, J. P., Piecuch, C. G., & Ross, A. C. (2024). A Link
- between U.S. East coast sea level and North Atlantic subtropical ocean heat content. Journal of
- Geophysical Research: Oceans, 129, e2024JC021425. https://doi. org/10.1029/2024JC021425
- 625 Souza, A. J., Simpson, J. H., Harikrishnan, M., & Malarkey, J. (2001). Flow structure and
- seasonalityin the Hebridean slope current. Oceanologica acta, 24, 63-76.
- Tebaldi, C., Ranasinghe, R., Vousdoukas, M., Rasmussen, D. J., Vega-Westhoff, B., Kirezci,
- 628 E., ... & Mentaschi, L. (2021). Extreme sea levels at different global warming levels. Nature
- 629 Climate Change, 11(9), 746-751.
- Tinker, J., Palmer, M. D., Harrison, B. J., O'Dea, E., Sexton, D. M., Yamazaki, K., & Rostron, J.
- W. (2024). Twenty-first century marine climate projections for the NW European shelf seas
- based on a perturbed parameter ensemble. Ocean Science, 20(3), 835-885.

- Tsimplis, M. N., & Rixen, M. (2002). Sea level in the Mediterranean Sea: The contribution of
- 634 temperature and salinity changes. Geophysical research letters, 29(23), 51-1.
- Tsimplis, M. N., & Shaw, A. G. (2008). The forcing of mean sea level variability around Europe.
- 636 Global and Planetary Change, 63(2-3), 196-202.
- Wahl, T., Haigh, I., Woodworth, P. L., Albrecht, F., Dillingh, D., Jensen, J., Nicholls, R. J.,
- Weisse, R., & Woppelmann, G. (2013). Observed mean sea level changes around the North Sea
- 639 coastline from 1800 to present. Earth Science Reviews, 124, 51–67.
- 640 https://doi.org/10.1016/j.earscirev.2013.05.003
- Wakelin, S. L., Holt, J. T., & Proctor, R. (2009). The influence of initial conditions and open
- boundary conditions on shelf circulation in a 3D ocean-shelf model of the North East Atlantic.
- 643 Ocean Dynamics, 59(1), 67-81.
- Weeks, J. H., Fung, F., Harrison, B. J., & Palmer, M. D. (2023). The evolution of UK sea-level
- projections. Environmental Research Communications, 5(3), 032001.
- 646 Uppala, S. M., Kållberg, P. W., Simmons, A. J., Andrae, U., Bechtold, V. D. C., Fiorino, M., ... &
- Woollen, J. (2005). The ERA-40 re-analysis. Quarterly Journal of the Royal Meteorological
- Society: A journal of the atmospheric sciences, applied meteorology and physical oceanography,
- 649 131(612), 2961-3012.
- Wise, A., Calafat, F. M., Hughes, C. W., Jevrejeva, S., Katsman, C. A., Oelsmann, J., ... &
- Richter, K. (2024). Using shelf-edge transport composition and sensitivity experiments to
- understand processes driving sea level on the Northwest European shelf. Journal of Geophysical
- 653 Research: Oceans, 129(5), e2023JC020587.
- Ku, X., Hurlburt, H. E., Schmitz Jr, W. J., Zantopp, R., Fischer, J., & Hogan, P. J. (2013). On the
- 655 currents and transports connected with the Atlantic meridional overturning circulation in the
- subpolar North Atlantic. Journal of Geophysical Research: Oceans, 118(1), 502-516.
- Krait Xu, X., Rhines, P. B., Chassignet, E. P., & Schmitz Jr, W. J. (2015). Spreading of Denmark Strait
- overflow water in the western subpolar North Atlantic: Insights from eddy-resolving simulations
- with a passive tracer. Journal of Physical Oceanography, 45(12), 2913-2932.

- Ku, X., Rhines, P. B., & Chassignet, E. P. (2018). On mapping the diapycnal water mass
- transformation of the upper North Atlantic Ocean. Journal of Physical Oceanography, 48(10),
- 662 2233-2258.
- Yin, J., Schlesinger, M. E., & Stouffer, R. J. (2009). Model projections of rapid sea-level rise on
- the northeast coast of the United States. Nature Geoscience, 2(4), 262-266.
- Yin, J., Griffies, S. M., & Stouffer, R. J. (2010). Spatial variability of sea level rise in twenty-first
- century projections. Journal of Climate, 23(17), 4585-4607.
- Zaron, E. D., & Ray, R. D. (2023). Clarifying the distinction between steric and baroclinic sea
- surface height. Journal of Physical Oceanography, 53(11), 2591-2596.